nature communications

Article

https://doi.org/10.1038/s41467-024-54481-x

Prebiotic formation of enantiomeric excess D-amino acids on natural pyrite

Received: 10 February 2024

Accepted: 8 November 2024

Ruiqi Li[1,3], Quanzheng Deng[1,3], Lu Han[1], Tianwei Ouyang[2], Shunai Che[1,2] & Yuxi Fang[2]

D-amino acids, found in excess in a minority of organisms and crucial for marine invertebrates, contrast with the more common L-amino acids in most life forms. The local prebiotic origin of D-amino acid enantiomeric excess in natural systems remains an unsolved conundrum. Herein, we demonstrate the formation of enantiomeric excess (*ee*) D-amino acids through photocatalytic reductive amination of α-keto acids on natural pyrite. Various amino acids with *ee* values in the range of 14.5–42.4%, are formed. The wavy arrangement of atoms on the surface of pyrite is speculated to lead to the preferential formation of D-amino acids. This work reveals the intrinsic asymmetric photocatalytic activity of pyrite, which could expand understandings on mechanism of asymmetric catalysis and chirality of inorganic crystals. Furthermore, it provides a plausible pathway for the prebiotic formation of D-amino acids, adding further evidence to the origin of D-amino acids enantiomeric excess in natural systems.

In the majority of living organisms, L-amino acids dominate as the primary building blocks of proteins and polypeptides[1] (Supplementary Fig. 1a). It is widely accepted that the excess of L-amino acids would be initially formed prebiotically, and subsequently, their concentration would be increased due to a shift in equilibrium that favors the production of L-amino acids, resulting in their overabundance[2]. For the initial formation of excess of L-amino acids, there are many factors on the primitive Earth that lead to chiral bias, including circularly polarized light[3], geomagnetic fields[4], vortices[5], chiral mineral surfaces[6–9], and chiral substances carried by extraterrestrial meteorites[10,11]. The chiral biases produced by these naturally occurring chiral factors can be further enhanced through chiral amplification, a phenomenon that is possibly exemplified by the Soai reaction[12] and the chiral amplification process during amino acid crystallization[13]. The studies mentioned above provide a reasonable hypothesis for the origins of life on Earth. The random D-amino acids enrichment could be initiated by chiral bias[3–11] or as a remnant from the prebiotic formation of L-peptides[14] if the reaction starts from a racemic or near-racemic solution. However, it remains a question why a minority of organisms exhibit an enantiomeric excess of D-amino acids following extensive chiral selection and amplification of L-amino acids on primitive Earth.

On the other hand, enantiomeric excess D-amino acids have recently been discovered in various minority of organisms and play important physiological roles[15–18](Supplementary Fig. 1b). A large number of free D-amino acids, including D-serine (Ser), D-alanine (Ala), D-proline (Pro), D-Glutamic Acid (Glu), D-Aspartic Acid (Asp), etc., were found in some bacteria, among which the *ee* values of D-Ala in *Lactobacillus sake*, *Lactobacillus delbrueckii* and *Lactobacillus curvatus* reached 18.4, 27.0 and 58.0%, respectively, and the *ee* value of D-Asp in *Brevibacterium linens* was 20.6%[19]. The *ee* values of free D-Ala and D-Asp can reach up to 29 and 40% in the tissues of certain marine invertebrates[20,21]. These D-amino acids act as crucial osmolytes for intracellular osmoregulation, participating in the regulation of osmotic balance against salinity changes[21–24]. In the pupae of silkworms and other species of the order *Lepidoptera* D-Ser with 30% *ee* was detected[15]. In the L-amino acid-dominated biological world, trace amounts of D-amino acids are known to function as neurotransmitters in animals and humans, and alterations in their metabolism may be linked to the

---

[1]School of Chemical Science and Engineering, Tongji University, Shanghai, China. [2]School of Chemistry and Chemical Engineering, Frontiers Science Center for Transformative Molecules, State Key Laboratory of Composite Materials, Shanghai Key Laboratory for Molecular Engineering of Chiral Drugs, Shanghai Jiao Tong University, Shanghai, China. [3]These authors contributed equally: Ruiqi Li, Quanzheng Deng. e-mail: chesa@sjtu.edu.cn; sjtu15901600323@sjtu.edu.cn

pathogenesis of various diseases[25]. Therefore, D-amino acids in these organisms are regarded as potential products of racemase activity or metabolites produced by the organisms themselves[26], with their biological sources in mammals being extensively reported[27,28]. However, the evidence supporting the prebiotic origin of enantiomeric excess of the D-amino acids in the ecosystem of modern life with low random factors has not been investigated (Supplementary Fig. 1b).

Herein, our approach is to explore the photocatalytic synthesis of enantiomeric excess D-amino acids on the surface of natural minerals for investigating the possible origin of D-amino acids in natural systems (Fig. 1, Supplementary Fig. 1b and Supplementary Dataset 1). It is well known that hydrothermal systems, found on land or underwater where geothermally heated water discharges, are considered potential environments for the emergence of life, especially in deep-sea vents and shallow-sea hydrothermal vents, with fluids enriched in transition metal elements, H_2S, NH_3, CO_2, CO and etc.[29–31]. Iron, the most abundant element among all transition metals, is initially predicted to form ferrous hydroxide, which undergoes sulfidation to subsequently form ferrous sulfide. This compound is then oxidized by H_2S to produce pyrite[32,33]. Pyrite, recognized as the most common sulfide mineral (cubic FeS_2), is widely distributed in marine systems and on the primitive Earth's surface[34], occurring not only as rock deposits but also as small particles (0.01–0.2 mm) within volcaniclastic sediments that are dispersed in seawater[35,36]. The pyrite crystal is known to have S-S bonds as an asymmetric factor[34], evidence for either chirality or enantioselectivity of pyrite has not been revealed yet, even though it is not a crystal with a chiral space group. Due to its suitable band gap for the generation of photoelectrons (e^-)[37,38], pyrite could potentially function as a semiconductor photocatalyst[39,40] when exposed to the Earth's surface or shallow water layers[39].

Pyruvic acid and other α-keto acids have been suggested to be a key intermediate in the prebiotic reduction and fixation of CO_2 via the reductive tricarboxylic acid (rTCA) or acetyl-CoA pathways[41,42]. Reductive amination of pyruvic acid to form Ala has been observed on mineral surfaces under simulated hydrothermal vent conditions[43]. Here, photocatalytic reductive aminations of α-keto acids were selected to investigate the enantioselectivity of the prebiotic synthesis of amino acids on the natural pyrite, as the last and crucial step to generate chiral centers of amino acids. The reductive amination reaction starts with a condensation step during α-keto acids react with ammonia, forming the corresponding imine, and then the imine is reduced by photoelectron (e^-) on the pyrite surface to the amino acids[44]. The various D-form enantiomeric excess amino acids would be formed due to the different adsorption energy (E_{ads}) of antipodal amino acids on the wavy arrangement of atoms on the surface of pyrite.

Naturally occurring samples of pyrite crystals from the England pyrite mine were acquired from Alfa Aesar (China) Chemical Co. Ltd. The natural pyrite was meticulously ground and sieved to achieve uniform dispersion in the reaction solution, which included α-keto acids and ammonia. To mitigate potential interference from microbial biochemical activities during the reaction process, the ground pyrite underwent sterilization using UV irradiation in an inert atmosphere. Furthermore, all reaction vessels were boiled in distilled water to guarantee sterility.

Results and Discussion

Characterization of natural pyrite

Single crystal X-ray diffraction (SCXRD) analysis of natural pyrite reveals a cubic crystal structure with space group *Pa*−3 and lattice parameters of $a = 5.4186$ nm (Fig. 2a and Supplementary Dataset 2). As shown in Fig. 2b$_1$, the natural pyrite is similar to a NaCl-type crystal structure, in which Fe atoms are located at both the vertices and face-centered points of the cube. Specifically, S_2^{2-} groups replacing Cl atoms are located at the edge and body-centered positions, and the arrangement of dumbbell-shaped S_2^{2-} groups reduces the symmetry of the crystal. Due to the low symmetry, the pyrite crystal is considered to possibly exhibit chirality[34], even though it is not a crystal with a chiral space group.

As shown in Fig. 2b$_2$, a wavy arrangement of Fe atoms and S atoms on the (200) crystal surface is observed. A wide-angle powder XRD pattern (Supplementary Fig. 2) of crushed natural pyrite used in photocatalysis shows that the reflections can be well indexed to the pure

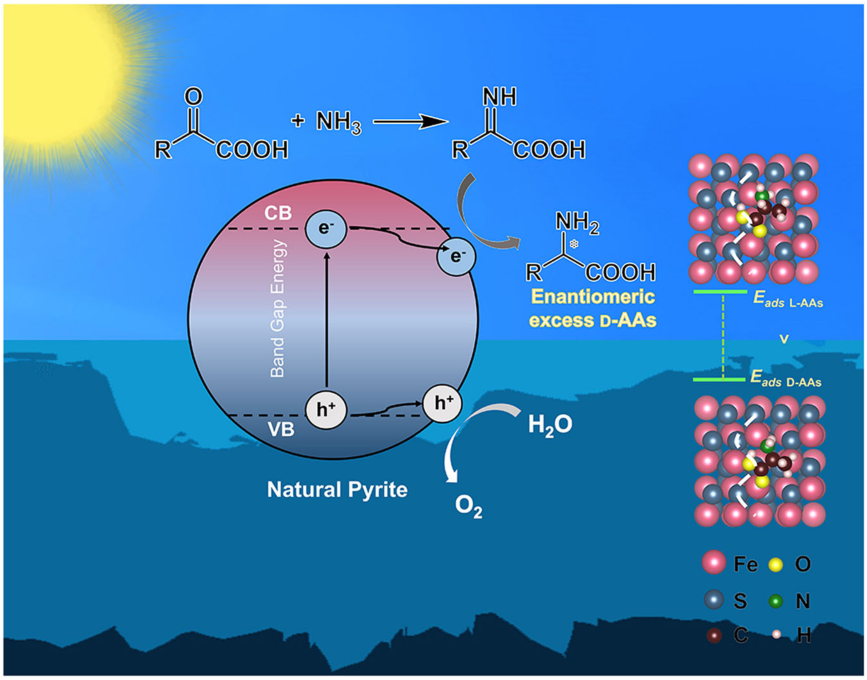

Fig. 1 | Schematic illustration of investigation strategy for the formation of D-amino acids on natural pyrite. The adsorption energies of L-amino acids (L-AAs) and D-amino acids (D-AAs) on the surface of pyrite were labeled as $E_{ads\ L\text{-}AAs}$ and $E_{ads\ D\text{-}AAs}$, respectively. The valence band and conduction band of natural pyrite were labeled as VB and CB, respectively.

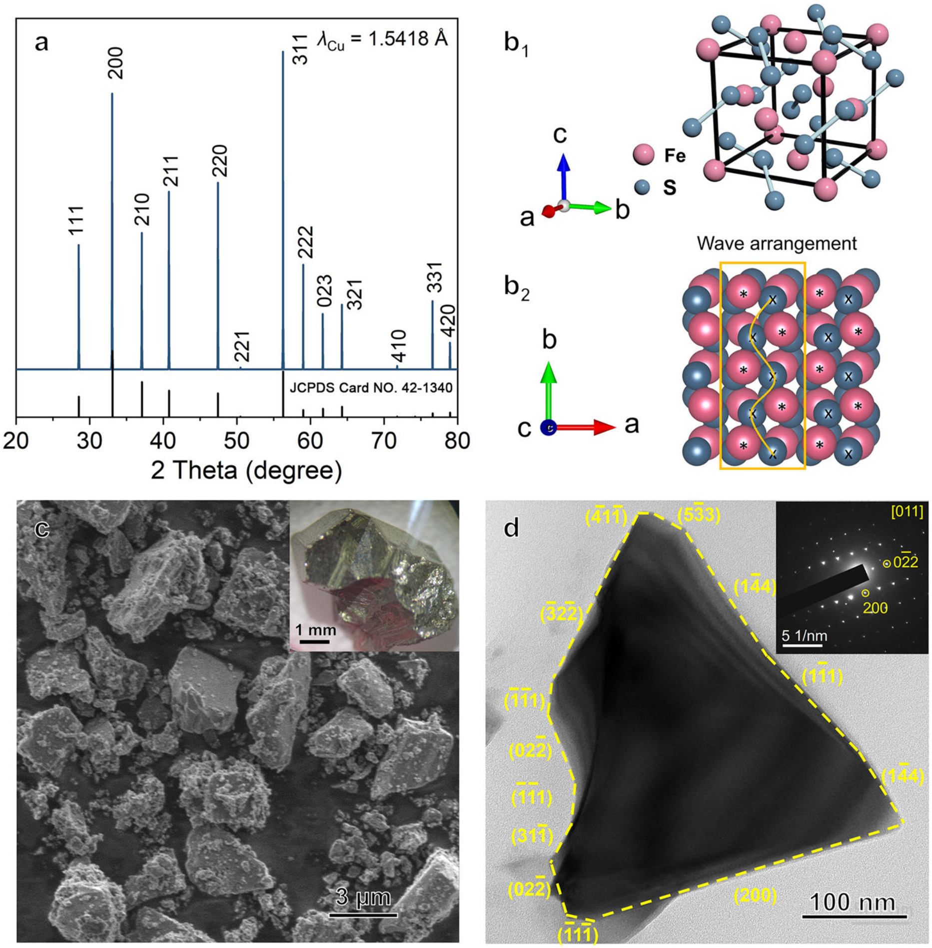

Fig. 2 | Morphology and structure of natural pyrite. a SCXRD pattern of natural pyrite. **b$_1$** Crystal structure of natural pyrite. **b$_2$** Atomic model of (200) with a wavy arrangement of Fe (pink spheres) and S (blue spheres) atoms. **c** SEM image of crushed natural pyrite and optical photograph (in set) of original natural pyrite particles. **d** TEM image and SAED image (in set) of natural pyrite, displaying mostly exposed crystal faces of {111}, {200}, and {220}. Source data are provided as a Source Data file.

cubic phase of FeS_2 (JCPDS Card No. 42-1340). In the reflections of all samples no additional peaks for other mineral impurities were observed. Scanning electron microscopy (SEM) image (Fig. 2c) of the sample obtained by crushing natural pyrite (inset of Fig. 2c) shows irregular morphology of pyrite crystals with sizes ranging from ~2 to ~10 μm.

The high-angle annular dark-field scanning transmission electron microscopy (HAADF-STEM) has been employed (Supplementary Fig. 3). Due to the high sensitivity of HAADF-STEM to the atomic numbers, it can be expected that Fe atoms could be observed with higher intensity (brightness). The 4-fold symmetry can be recognized from most parts of samples, suggesting the [001] axis. The transmission electron microscopy (TEM) images of natural pyrite show the single crystalline feature of the mineral particles (Fig. 2d and Supplementary Fig. 4), in which the crystal surfaces are labeled in the perpendicular direction of the particles. The top and bottom surfaces of the particles, as well as the inclined crystal surfaces, could not be fully assessed. Judging from the corresponding crystal morphology and the selected area electron diffraction (SAED) pattern, all exposed crystal faces can be assigned to the low-index lattice, among which {111}, {200}, and {220} were mostly observed. This finding suggests that these three crystal surfaces are exposed in most natural pyrite particles.

Photocatalytic reductive amination of α-keto acids on natural pyrite

Crushed particles of natural pyrite were dispersed through ultrasonication in solutions containing α-keto acids and ammonia. Subsequently, the mixture was exposed to Xe lamp irradiation to produce various amino acids. The reactions took place in a closed double-walled reactor with a quartz glass window allowing the passage of incident light (Supplementary Fig. 5). Pyruvic acid (mw: 88.06), 4-methyl-2-oxovaleric acid (mw: 130.14), 2-ketoglutaric acid (mw: 146.10) and 3-phenylpyruvate (mw: 164.16) were selected as the substrates of Ala, isoleucine (Ile), Glu and phenylalanine (Phe) in the sequence of increasing molecular weight. Pyruvic acid was selected as the model substrate to evaluate the feasibility of the photocatalytic reductive amination of α-keto acids on natural pyrite (Supplementary Fig. 6-10 and Supplementary Table. 3-4). Optimized reaction conditions were established, the 2 ml water containing 40 μmol of α-keto acids, 4 mmol of ammonia and 10 mg of natural pyrite, with irradiation of a Xe lamp at 20 °C for 24 hours.

As shown in Fig. 3a, Ala, Ile, Glu, and Phe with yields of 713, 555, 395, and 23 nmol were synthesized from photocatalytic amination of corresponding α-keto acids, respectively. The yield of amino acids is decreased briefly with increasing molecular weight of corresponding α-keto acids, which would be related to the solubility of their substrates. The solubility of pyruvic acid, 4-methyl-2-oxovaleric acid, 2-ketoglutaric acid and 3-phenylpyruvate are *ca.* 44, 27, 10, and <0.01 g/100 g water, respectively.

The *ee* value of amino acids produced with natural pyrite was determined by high-performance liquid chromatography-tandem mass spectrometry (HPLC-MS) after derivatization by *N*-(5-fluoro-2,4-dinitrophenyl)-L-leucinamide (L-FDLA). To eliminate the chiral bias of

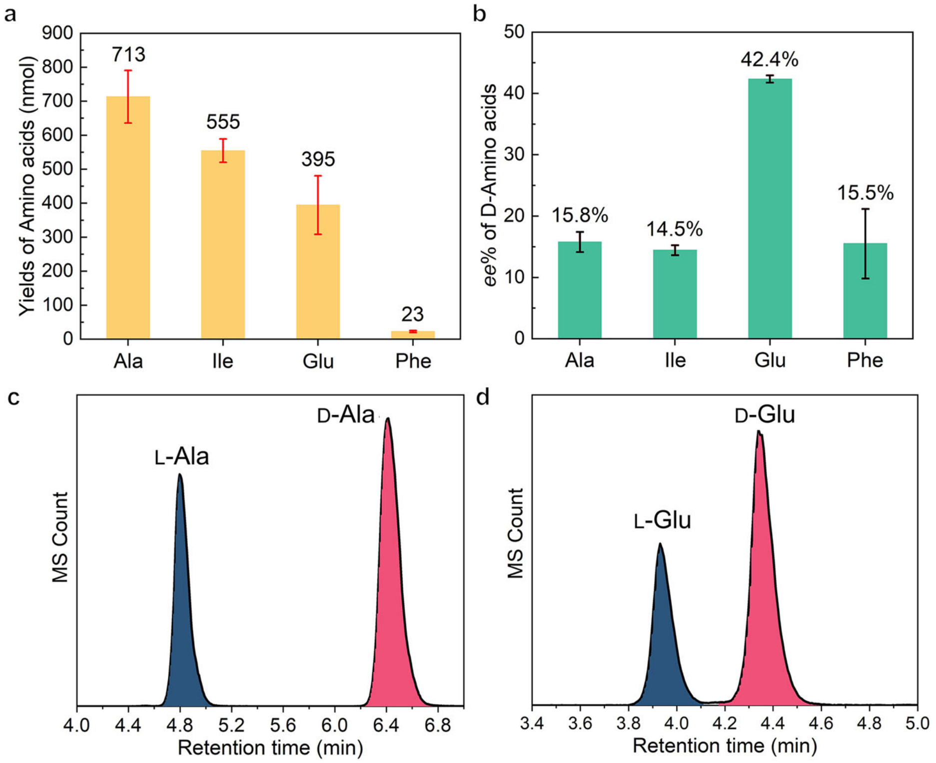

Fig. 3 | Formation of various amino acids through the photocatalytic reductive amination of corresponding α-keto acids on natural pyrite. a Yields of various amino acids (Ala: alanine, Ile: isoleucine, Glu: glutamic acid, Phe: phenylalanine). **b** *ee* values of D-amino acids corresponding to Fig. 3a. The detailed results of each repeated experiment are listed in the Supplementary Information (Supplementary Table 5). **c, d** HPLC-MS of Ala and Glu obtained from the photocatalytic reduction of pyruvic acid and 2-ketoglutaric acid, respectively. Reactions were carried out with a composition of 40 μmol α-keto acids, 4 mmol ammonia, 2 ml H_2O and 10 mg natural pyrite, and with irradiation of a Xe lamp at 20 °C for 24 hours. Error bars represent the standard deviations calculated from three independent photocatalytic experiments. Source data are provided as a Source Data file.

the L-FDLA derivatization method for amino acid enantiomers, all *ee* values were corrected using the corresponding standard curve (Supplementary Fig. 11). As shown in Fig. 3b, Ala, Ile, Glu, and Phe with 15.8, 14.5, 42.4 and 15.5% *ee* values of D-form were synthesized, respectively. The *ee* values of D-amino acids produced on the surface of pyrite are similar to those observed in certain marine invertebrates[20,21] and bacteria[19]. Figure 3c and d show the HPLC-MS spectra of Ala and Glu obtained from natural pyrite. The retention time of L-Ala and D-Ala were approximately 4.80 and 6.41 min, and the retention time of L-Glu and D-Glu were approximately 3.92 and 4.32 min, respectively (Others were shown in Supplementary Fig. 12).

To further mitigate the chiral effects caused by both the vortex[40] and the magnetic field generated and introduced by the magnetic stirrer, the photocatalytic reaction was carried out without stirring. Manual shaking was employed instead of magnetic stirring. As anticipated, the yield was lower than that of experiments with stirring due to the ineffective dispersion of catalysts, while the enantiomeric excess (*ee*) value of the product was similar to that of the reaction under stirring (Supplementary Table 4). This result indicates that the enantioselectivity of the products was not influenced by the chiral effects of the vortex generated by stirring and the magnetic field of the stirrer. Other potential sources of chirality were also excluded through a series of control experiments (Supplementary Tables 6-7 and Supplementary Figs. 13–15).

Temperature-programmed desorption (TPD) of antipodal amino acids on natural pyrite

Enantiospecific interactions between chiral molecules and chiral surfaces manifest as differences in adsorption energies[22]. To investigate the enantioselective mechanism of the pyrite surface, the adsorption energies of amino acids on natural pyrite surfaces were studied through TPD approach. As shown in Fig. 4a, the desorption peak for D- and L-Ala appeared at ~297 and ~280 °C, respectively. Similarly, the TPD peaks of D- and L-Glu appeared at ~499 and ~488 °C, respectively (Supplementary Figs. 16 and 17). The desorption temperatures of the D-form were consistently higher than those of the L-form, indicating that D-amino acids adopt a more stable adsorption conformation on the pyrite surface than L-amino acids. Consequently, D-amino acids require higher energy for desorption than L-amino acids. Thus, the enantioselectivity of D- and L-amino acids on the pyrite surface was experimentally validated through differences in adsorption energies.

Density functional theory (DFT) calculations for the enantioselectivity of Ala on the surface of natural pyrite

DFT calculations of the adsorption energies of D- and L-Ala on various crystal surfaces was performed to investigate the mechanism underlying enantioselectivity on the surface of pyrite (Supplementary Dataset 3). The 3*d* orbitals of Fe atoms in pyrite split into two groups: t_{2g} (dxy, dxz, and dyz) and e_g (dz_2 and dx_2-y_2), forming the valence band (VB) and conduction band (CB), respectively[45,46]. The CB (t_{2g}) is entirely occupied by six 3*d* electrons of Fe^{2+} cations, resulting in the non-magnetic ground state of pyrite[47–49]. Therefore, the calculations have been carried out without spin polarization. To avoid the impact of amino acids orientation on binding energy in the adsorption models, both D- and L-amino acids were randomly positioned at three different locations in all adsorption models (using D- and L-Ala as examples, see Supplementary Figs. 18 and 19).

Figure 4b shows the adsorption energies of D- and L-Ala on the (111), (200) and (220) surfaces (Supplementary Table 8). The adsorption energies of Ala on the (200) and (220) surfaces were lower than

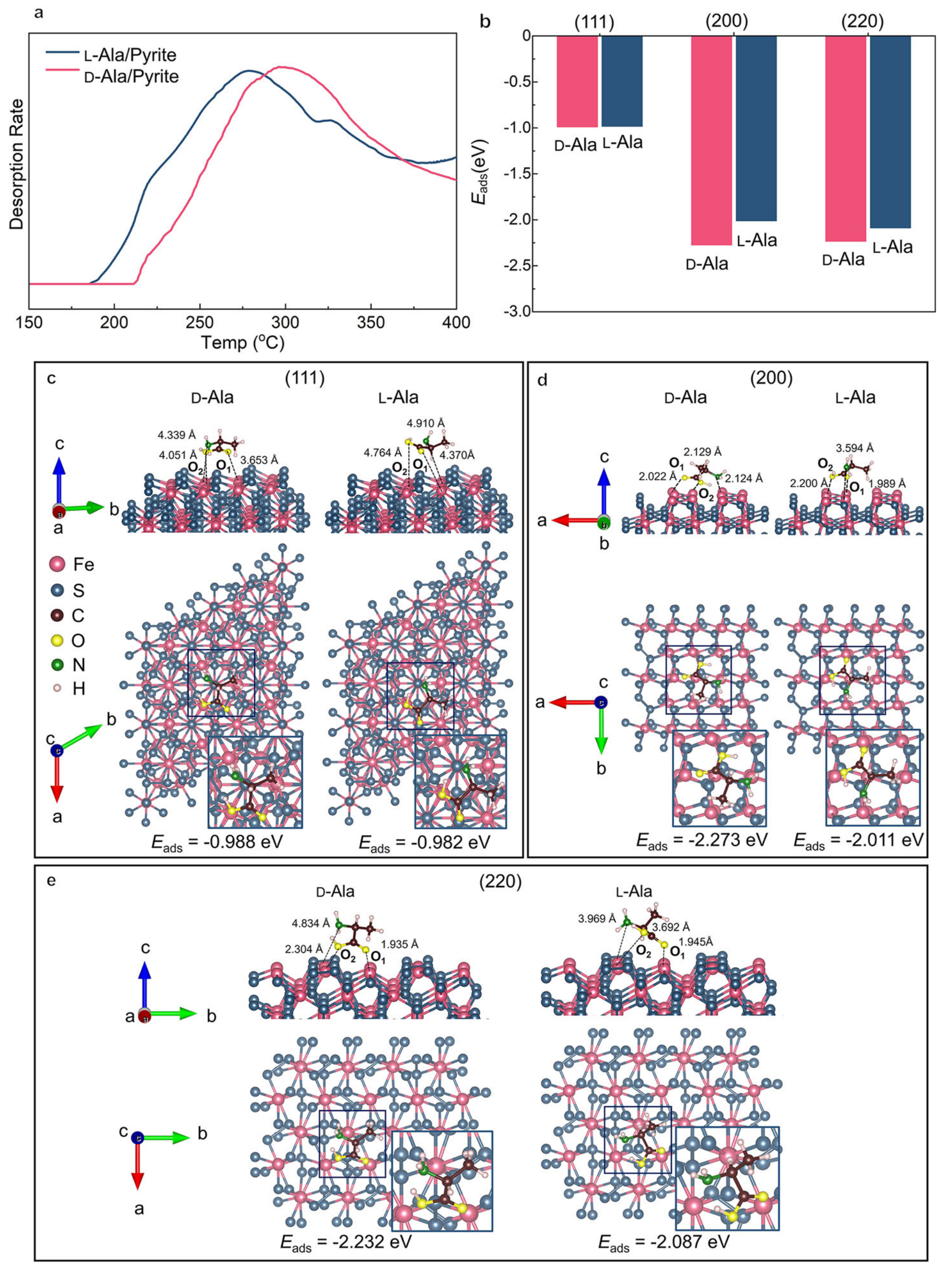

Fig. 4 | Adsorption energies of D- and L-alanine (Ala) on natural pyrite surface, studied by TPD and DFT calculations. a TPD profiles of D- and L-Ala on the natural pyrite surface. **b** The comparison of adsorption energy differences between D- and L-Ala on different crystal surfaces. **c**–**e** The adsorption models of D- and L-Ala on the various crystal surfaces: (111), (200), and (220). The adsorption energy was labeled as E_{ads}. Source data are provided as a Source Data file.

that on the (111) surface, indicating that the adsorption effect of Ala on the (200) and (220) surfaces is stronger than on the (111) surface. The same trends of $E_{ads\ \text{D-Ala}} < E_{ads\ \text{L-Ala}}$ suggest that D-Ala adsorption is energetically favored over the L-Ala on the pyrite surface. Specifically, on the (200) crystal surface with a wavy arrangement of Fe atoms and S atoms, the adsorption energy difference between D-Ala and L-Ala molecules is maximized. With D-Ala displaying a lower adsorption energy and a more stable adsorption configuration, thereby indicating a favorable affinity with natural pyrite compared to L-Ala. The difference of adsorption energy was explained by adsorption behaviors of Ala as shown in Fig. 4c–e, in which the oxygen atoms of -C=O and -OH in -COOH of Ala are denoted as O_1 and O_2, respectively.

As shown in Fig. 4c, on the (111) crystal surface, the position of the S atom on the topmost layer makes it challenging to establish an effective coordination interaction with the Ala molecule. The adsorption energies E_{ads} for D-Ala and L-Ala were −0.988 and −0.982 eV, respectively, indicating the weakest adsorption capacity for Ala. The distance between the molecule and the crystal surface is relatively large (>3.6 Å), providing evidence of a higher adsorption energy and an unstable adsorption effect.

On the (200) surface (Fig. 4d), two oxygen atoms of the carboxyl group in Ala are adsorbed onto two adjacent Fe atoms arranged in a wavy pattern along the *b*-axis, with Fe--O_1 = 2.129 Å and Fe--O_2 = 2.022 Å in D-Ala and Fe--O_1 = 1.989 Å and Fe--O_2 = 2.200 Å in L-Ala, respectively. The distances from the carboxyl group to the crystal surface are similar in D- and L-Ala, while the distances between amino group with Fe atom are significantly different. The Fe--N = 2.124 Å and 3.594 Å in D- and L-Ala, respectively, due to the smaller steric hindrance of D-Ala observed from the adsorption configuration. The interaction between amino group with Fe atom in L-Ala is significant weaker than that in D-Ala, due to the greater steric hindrance caused by the H atoms at C_2, which results in the adsorption energies of D-Ala lower than L-Ala, with $E_{ads\ \text{D-Ala}} = -2.273$ eV and $E_{ads\ \text{L-Ala}} = -2.011$ eV, respectively. On the (200) surface, the adsorption energies of Ala are lower than on (111). The above results indicate that the wavy arrangement of Fe atoms on the (200) surface provides a stronger affinity and enantioselective interaction with chiral amino acids.

On the (220) surface, oxygen atoms adsorb onto two adjacent Fe atoms, arranged in a straight line along the *b*-axis (Fig. 4e), with Fe--O_1 = 1.935 Å, Fe--O_2 = 2.304 Å and Fe--N = 4.834 Å in D-Ala and Fe--O_1 = 1.945 Å, Fe--O_2 = 3.692 Å and Fe--N = 3.969 Å in L-Ala, respectively, which resulted in similar $E_{ads\ \text{D-Ala}} = -2.232$ eV and $E_{ads\ \text{L-Ala}} = -2.087$ eV, respectively. These adsorption energies are similar to that on (200) due to similar adsorption behaviors of Ala with Fe atoms. The difference between these adsorption energies is smaller than that on (200). Although the Fe atoms are arranged in a straight line, the surrounding S atoms with a wavy arrangement, leading to a weaker enantioselective interaction with chiral amino acids on (220) surface.

The adsorption energies of D- and L-Ala on (211) observed in TEM (Fig. 2d) were calculated to be $E_{ads\ \text{D-Ala}}$ and $E_{ads\ \text{L-Ala}}$ of −2.261 eV and −1.923 eV, respectively (Supplementary Fig. 20). Although both D- and L-Ala were adsorbed on the (211) crystal surface trough a single oxygen atom, with Fe--O_1 = 1.943 Å in D-Ala and Fe--O_2 = 1.975 Å in L-Ala, leading to an evidently enantioselective interaction with chiral amino acids on (211) surface.

The above results suggest that the wavy arrangement of Fe atoms on crystal surfaces plays a crucial role in the enantioselective adsorption of amino acids. This simulation reasonably explains the excessive production of D-amino acids on the surface of pyrite. These results fundamentally elucidate that the enantiomeric excessed formation of D-amino acids on natural pyrite is a consequence of the inherent atomic arrangement on pyrite crystal surfaces.

DFT calculations for the different *ee* values of Ala and Glu formed on (200) surface

To comprehend the formation of Glu with a higher *ee* value than Ala, we employed DFT calculations to assess the Gibbs free energy for each formation pathway (Supplementary Dataset 3). The (200) crystal surface was selected as the model due to its demonstrated effective enantioselectivity, as confirmed above (Fig. 4b).

Fig. 5a_1 and b_1 show pathways for Ala and Glu formation (Supplementary Dataset 1) based on the mechanism of photocatalytic synthesis for amino acids[44]. Pyruvic acid and 2-ketoglutaric acid reacted with ammonia, forming the corresponding imines, and then the imines were reduced to form Ala and Glu, respectively. Fig. 5a_2 and b_2 show the Gibbs free energy profiles for the intermediates in two pathways (Supplementary Table 9), respectively. The reduction of imine to corresponding amino acids was the crucial stereoselective step. The difference in Gibbs free energies for the formation of D- and L-Glu on (200) surface is 0.869 eV significantly higher than that of 0.344 eV difference in D- and L-Ala (Supplementary Tables 10 and 11), which accounts for the higher enantioselectivity in the formation of Glu on the pyrite surface than Ala.

These differences can be explained in the terms of adsorption behaviors of Ala and Glu on natural pyrite surface. The two -COOH groups in antipodal Glu are adsorbed on the (200) surface with two non-adjacent Fe atoms in similar way. The distances are Fe--O_1 = 2.012 Å and Fe--O_2 = 2.005 Å in D-Glu and Fe--O_1 = 2.007 Å and Fe--O_2 = 2.015 Å in L-Glu, respectively (Fig. 5b_3 and Supplementary Fig. 21). On the other hand, the distances between the amino group and Fe atom are Fe--N = 2.056 and 4.060 Å in D- and L-Glu adsorbed on pyrite surface, respectively (Supplementary Table 12). The differences of distance between amino groups of antipodal Glu and Fe atoms is 2.004 Å much larger than that 1.470 Å of Ala (Fig. 5a_3), corresponding to differences in their enantioselectivity. Based on the theoretical calculations, it is hypothesized that the higher *ee* value of Glu than Ala might be due to the dual -COOH groups of Glu making its enantiomeric adsorbate configurations more different from one another than the Ala configurations.

In summary, a variety of biologically relevant amino acids with enantiomeric excess of the D-form were prebiotically photosynthesized on the natural pyrite surface, unaffected by chiral environments such as vortices or magnetic fields. According to DFT calculations, the wavy arrangement of atoms on the surface of pyrite

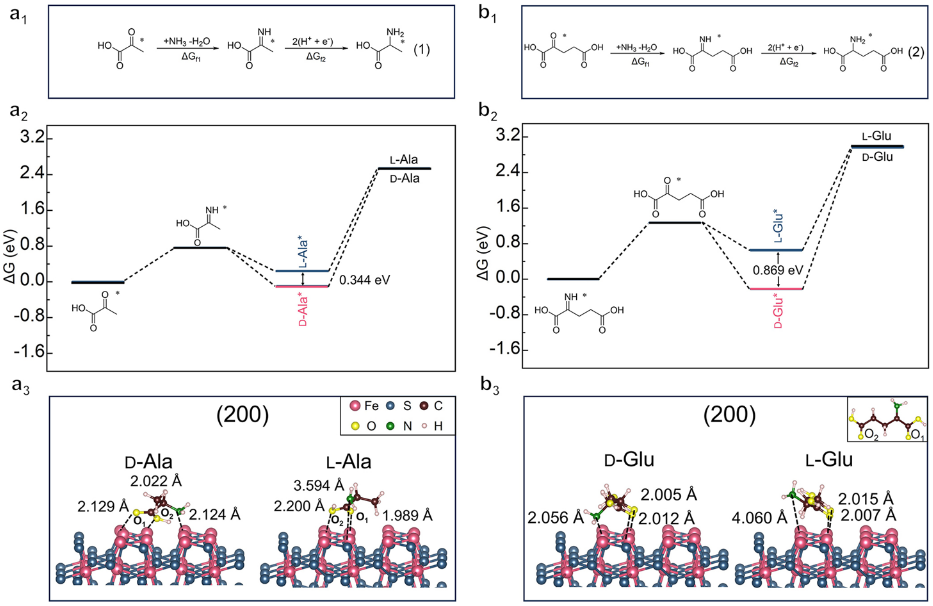

Fig. 5 | DFT calculations for the enantioselective formation of alanine (Ala) and glutamic acid (Glu). **a_1** Pathway of Ala formation from pyruvic acid and NH_3. **a_2** Gibbs free energy profile of the intermediates for the formation of D-/L-Ala on (200) surface of natural pyrite. **a_3** Calculated models for Ala enantiomers on pyrite crystal surface (200). **b_1** Pathway of Glu formation from 2-ketoglutaric acid and NH_3. **b_2** Gibbs free energy profile of the intermediates for the formation of D-/L-Glu on (200) surface of natural pyrite. **b_3** Calculated models for Glu enantiomers on pyrite crystal surface (200). The Gibbs free energy was labeled as ΔG. Source data are provided as a Source Data file.

was speculated to lead to the preferential formation of D-amino acids, attributed to their stronger affinity resulting from smaller steric hindrance in the adsorption structure compared to L-amino acids, which led to the lower adsorption energies of the D-form compared to their enantiomers. Intrinsic enantioselectivity of pyrite surfaces originating from S-S bonds in lattices was revealed in our work, which reveals source of inorganic chirality other than chiral space group and chiral nanostructure. Based on this discovery, it can be further concluded that there is one of possible D-amino acids scenario that D-amino acids independently evolve on pyrite surfaces generated from hydrothermal vents, while L-amino acids become major species on the primitive Earth. The work provides the alternative possibility of explaining the origin of D-amino acids in modern life with fewer random factors involved.

Methods

Morphology and structural characterizations of the catalyst

SCXRD data were collected at 295 K using Cu-Kα radiation ($\lambda = 1.54178$ Å) from a fine-focus sealed tube operating at 50 kV and 50 mA on a BRUKER D8 VENTURE diffractometer equipped with a PHOTON II detector.

Powder XRD patterns were recorded on a Rigaku MiniFlex 600 powder diffractometer equipped with Cu Kα radiation (40 kV, 15 mA), at a rate of 0.2° min^{-1} over the range of 20–80°.

SEM was conducted on a JEOL JSM-7100F electron microscope operating at 2 kV.

HRTEM images were obtained using a JEOL model JEM-2100F operated with a field-emission gun at 200 kV. Aberration-corrected scanning transmission electron microscopy (AC-STEM) was performed using a probe-corrected Hitachi HF5000 S/TEM, operating at 200 kV. The instrument was equipped with bright field (BF), HAADF and secondary electron (SE) detectors for high spatial resolution STEM imaging experiments.

TEM images were taken with a JEOL JEM-F200 TEM microscope operated at 200 kV. Images were recorded using a Gatan OneView IS camera.

Photocatalytic reductive amination on pyrite

Millipore water used in all reactions was fed N_2 for 30 minutes to remove oxygen. Pyrite powder was added to the photocatalytic c with a quartz light window and a temperature-controlled water bath. Then the reactor was deoxygenated by purging N_2 for 10 minutes, after that the mixture of pyruvic acid (40 µmol) and NH_3•H_2O (0.28 ml, 28% wt) in 2 ml Millipore water was injected into the reactor. The reaction liquid is irradiated by a 500 W xenon lamp (SOFN Instruments CO., Ltd. 7ILX500) through the quartz light window for a certain time at 20 °C, the average light intensity irradiated on the photoreactor was *ca.* 180 mW cm^{-2}.The precipitates were removed by cooling and centrifugation.

Finally, the solution was lyophilized to remove water. The yields of amino acids were analyzed by amino acid analyzer (Supplementary Tables 1 and 2). The purified product was derivatized by L-FDLA before separation by HPLC-MS. To derivatize amino acid compounds, the product was dissolved in 500 µl of DI water, and then 50 µl of an aqueous solution was mixed with 20 µl of 200 mM sodium bicarbonate and 20 µl of 1% L-FDLA in acetone. The mixture was incubated at 37 °C for 30 min. After returning to room temperature, 200 µl of methanol was added to the sample, and the impurity was centrifuged (8049 g, 10 min). The sample was kept in a dark condition.

HPLC-MS analysis was performed by using an Acquity UPLC & XEVO G2-XS QTOF (Waters, United States) equipped with a UPLC column (Acquity UPLC HSS T3 1.8 µm, 2.1*100 mm). The detection of samples was conducted in positive ESI mode, and the function type was TOF-MS with a mass range of 200–600. Then, a 0.1 µl sample was injected and eluted using mobile phase A (0.1% mass concentration of formic acid aqueous solution) and mobile phase B (acetonitrile) at a flow rate of 0.35 ml/min. The programmed mobile phase gradient was as follows: 0.00–1.00 min, 25% B; 1.00–4.30 min 35% B; 4.30–6.50 min 100% B; 6.50–40 min 25% B. The column was equilibrated prior to sample injection, and the temperature of the column oven was set at 45 °C.

To generate a standard curve of L- and D-Amino acids (AAs), the standard compounds were diluted in water at concentrations adjusted to be relevant to product contents. After derivatization, 10 µl of the standard solution was separated and detected using the HPLC-MS system.

The enantiomeric excess (*ee*) was calculated based on the integrated peak areas of L- and D-AAs as indicated in Eq. 3.

$$ee = (\mathrm{l} - \mathrm{AAs} - \mathrm{d} - \mathrm{AAs})/(\mathrm{l} - \mathrm{AAs} + \mathrm{d} - \mathrm{AAs}) \tag{3}$$

where L-AAs and D-AAs represent the obtained peak areas of L-FDLA-derivatized L-AAs and L-FDLA-derivatized D-AAs, respectively. The standard error of the mean of the %*ee* was calculated by means of Eq. 4.

$$\text{s.e.m.} = S/n \tag{4}$$

where *S* is the standard deviation and *n* is the number of experiments.

Temperature-programmed desorption

In the TPD analysis of D-/L-Ala and D-/L-Glu on natural pyrite, 50 mg of crushed pyrite particles were added to 5 ml of D-Ala, L-Ala, D-Glu and L-Glu standard solutions with a concentration of 2.5 mg/ml, respectively. The mixture was vigorously stirred for 1 hour at room temperature. Subsequently, the pellet was centrifuged in a high-speed centrifuge at 8049 g for 5 minutes, following which the supernatant was removed as much as possible. Then, the remaining solids were rapidly rinsed twice with deionized water to remove residual free amino acids as much as possible and dried in an oven at 60 °C overnight. The sample was sealed and subjected to the TPD test. The above process was independently repeated three times, and the mean of the three results was taken as the final outcome.

The TPD of amino acids adsorbed on natural pyrite was conducted under N_2 atmosphere using the Quantachrome Autosorb-iQ-C chemisorption analyzer. The species desorbing from the surface were monitored by the thermal conductivity detector.

Computational details

Density functional theory calculations were performed using the plane-wave-based Vienna Ab Initio Simulation package (VASP)[50]. The wavefunction was expanded in a plane-wave basis set with an energy cutoff of 480 eV. The electron exchange and correlation effects were described by the generalized gradient approximation (GGA) in the form of the Perdew–Burke–Ernzerhof (PBE) functional[51]. The D4 correction method was employed to illustrate the long-range dispersion interactions between the adsorbates, water, and pyrite surface[52]. The interaction between atomic cores and electrons was described by the projector augmented wave (PAW) method[51]. A cut-off energy of 480 eV for the plane-wave basis set and an atomic force convergence of 0.02 eV/Å were employed. A Fermi smearing width of 0.02 eV and dipole corrections were employed as well. For the calculation of all thermodynamic quantities, the open-source atomic simulation environment (ASE)[53] code was used. The Gibbs free energies were calculated at 298 K and 1 atm as outlined below:

$$G = H - TS = E_{DFT} + E_{ZPE} + \mathrm{C_p} - TS \tag{5}$$

where E_{DFT} is the DFT-calculated electronic energy, E_{ZPE} is the zero-point vibrational energy, Cp is the heat capacity, *T* is the temperature, and *S* is the entropy. Gas-phase molecules such as H_2 were treated using the ideal gas approximation, while adsorbates were treated using a harmonic approximation. The computational hydrogen electrode (CHE) model was used to calculate the Gibbs free formation energy for Ala, Glu, and imine intermediates[54]. For example, the Gibbs free energy of formation for $HOOCCNHCH_3^*$ was calculated as $G_f = G_{HOOCCNHCH3^*}$ - ($G_{HOOCCOCH3^*}$). The adsorption energy of each amino acid was calculated as $E_{ads} = E_{AA^*}$ - ($E_{slab} + E_{AA}$).

The whole reaction from pyruvic acid to Ala was proposed as follows:

$$HOOCCOCH_3^* + 2H^+ + NH_3 \rightarrow HOOCCNHCH_3^* + 2H^+ + H_2O \quad (6)$$

$$HOOCCNHCH_3^* + 2H^+ + H_2O \rightarrow HOOCHCNH_2CH_3^* + 2H^+ + H_2O \quad (7)$$

The whole reaction from pyruvic acid to Glu was proposed as follows:

$$HOOCCOCH_2CH_2COOH^* + 2H^+ + NH_3 \rightarrow HOOCCNHCH_2CH_2COOH^* + 2H^+H_2O \quad (8)$$

$$HOOCCNHCH_2CH_2COOH^* + 2H^+ + H_2O \rightarrow HOOCHCNH_2CH_2CH_2COOH^* + H_2O \quad (9)$$

The (111), (200), and (220) were modeled using (2×2) supercells with a (1 × 1 × 1) k-point grid ((1 × 1 × 1) k-point grid for small-molecule adsorptions). The (211) was modelled using (1 × 1) supercells with a (1 × 1 × 1) k-point grid ((1 × 1 × 1) k-point grid for small-molecule adsorptions). In addition, the models of the (111), (200), (220), and (211) have a 4-atom layer in the z-axis direction and a 25 Å vacuum slab between mirror images in the z-axis in the unit cell.

Data availability

The source data underlying Figs. 2a, 3c, d, 4a, 5a_2 and b_2 and Figures in SI are provided as a Source Data file, and other source data could be found in Supplementary Information (SI). Source data are provided with this paper.

References

1. Mason, S. Chemical evolution - origin of biomolecular chirality. *Nature* **314**, 400–401 (1985).
2. Bada, J. L. Origins of homochirality. *Nature* **374**, 594–595 (1995).
3. Sugahara, H. et al. D-amino acids in molecular evolution in space – absolute asymmetric photolysis and synthesis of amino acids by circularly polarized light. *Biochim. Biophys. Acta* **1866**, 743–758 (2018).
4. Rikken, G. L. J. A. & Raupach, E. Enantioselective magnetochiral photochemistry. *Nature* **405**, 932–935 (2000).
5. Ribó, J. M., Crusats, J., Sagués, F., Claret, J. & Rubires, R. Chiral sign induction by vortices during the formation of mesophases in stirred solutions. *Science* **292**, 2063–2066 (2001).
6. Hazen, R. M., Filley, T. R. & Goodfriend, G. A. Selective adsorption of L- and D-amino acids on calcite: implications for biochemical homochirality. *Proc. Natl Acad. Sci. USA.* **98**, 5487–5490 (2001).
7. Puisto, S. R. et al. The structure of the Chiral Pt531 surface: a combined LEED and DFT Study. *J. Phys. Chem. B* **109**, 22456–22462 (2005).
8. Fang, Y. et al. Synthesis of amino acids by electrocatalytic reduction of CO_2 on chiral Cu surfaces. *Chem* **9**, 460–471 (2023).
9. Fang, Y. et al. Enantiospecific affinities of chiral Cu films for both D-Ribose and L-amino acids. *Chem. Mater.* **35**, 2402–2407 (2023).
10. Chan, Q. H. S., Zolensky, M. E., Martinez, J. E., Tsuchiyama, A. & Miyake, A. Magnetite plaquettes are naturally asymmetric materials in meteorites. *Am. Mineral.* **101**, 2041–2050 (2016).
11. Pizzarello, S., Zolensky, M. & Turk, K. A. Nonracemic Isovaline in the Murchison meteorite: chiral distribution and mineral association. *Geochim. Cosmochim. Acta* **67**, 1589–1595 (2003).
12. Soai, K. et al. D- and L-quartz-promoted highly enantioselective synthesis of a chiral organic compound. *J. Am. Chem. Soc.* **121**, 11235–11236 (1999).
13. Breslow, R. & Levine, M. S. Amplification of Enantiomeric concentrations under credible prebiotic conditions. *Proc. Natl Acad. Sci. Usa.* **103**, 12979–12980 (2006).
14. Deng, M., Yu, J. & Blackmond, D. G. Symmetry breaking and chiral amplification in prebiotic ligation reactions. *Nature* **626**, 1019–1024 (2024).
15. Corrigan, J. J. D-amino acids in animals. *Science* **164**, 142–149 (1969).
16. Richter, K., Egger, R. & Kreil, G. D-Alanine in the Frog skin peptide Dermorphin is derived from L-Alanine in the precursor. *Science* **238**, 200–202 (1987).
17. Brückner, H. & Westhauser, T. Chromatographic determination of L- and D-amino acids in plants. *Amino Acids* **24**, 43–55 (2003).
18. Irazoki, O. et al. D-amino acids signal a stress-dependent run-away response in Vibrio Cholerae. *Nat. Microbiol.* **8**, 1549–1560 (2023).
19. Brückner, H., Becker, D. & Lüpke, M. Chirality of amino acids of microorganisms used in food biotechnology. *Chirality* **5**, 385–392 (1993).
20. D'Aniello, A. & Giuditta, A. Presence of D-aspartate in Squid Axoplasm and in other regions of the Cephalopod nervous system. *J. Neurochem.* **31**, 1107–1108 (1978).
21. Okuma, E., Fujita, E., Amano, H., Noda, H. & Abe, H. Distribution of free D-amino acids in the tissues of crustaceans. *Fish. Sci.* **61**, 157–160 (1995).
22. Nagata, Y. *Advances in BioChirality*, Chapter 19 - d-Amino Acids in Nature, 271-283 (Elsevier Science B.V., 1999).
23. Sasabe, J. & Suzuki, M. Distinctive roles of D-amino acids in the homochiral world: chirality of amino acids modulates mammalian physiology and pathology. *Keio J. Med.* **68**, 1–16 (2018).
24. Abe, H., Okuma, E., Amano, H., Noda, H. & Watanabe, K. Role of free D- and L-Alanine in the Japanese Mitten Crab Eriocheir Japonicus to intracellular osmoregulation during downstream spawning migration. *Comp. Biochem. Physiol., Part A: Mol. Integr. Physiol.* **123**, 55–59 (1999).
25. Fuchs, S. A., Berger, R., Klomp, L. W. J. & de Koning, T. J. D-amino acids in the central nervous system in health and disease. *Mol. Genet. Metab.* **85**, 168–180 (2005).
26. Genchi, G. An overview on D-amino acids. *Amino Acids* **49**, 1521–1533 (2017).
27. Ollivaux, C., Soyez, D. & Toullec, J.-Y. Biogenesis of D-amino acid containing peptides/proteins: where, when and how? *J. Pept. Sci.* **20**, 595–612 (2014).
28. Fujii, N. D-amino acids in living higher organisms. *Orig. Life Evol. Biosph.* **32**, 103–127 (2002).
29. Camprubí, E. et al. The emergence of life. *Space Sci. Rev.* **215**, 56 (2019).
30. Barge, L. M. & Price, R. E. Diverse geochemical conditions for prebiotic chemistry in shallow-sea alkaline hydrothermal vents. *Nat. Geosci.* **15**, 976–981 (2022).
31. Bayraktarov, E., Price, R. E., Ferdelman, T. G. & Finster, K. The pH and pCO_2 dependence of sulfate reduction in shallow-sea hydrothermal CO_2 – venting sediments (Milos Island, Greece). *Front. Microbiol.* **4**, 111 (2013).
32. Drobner, E., Huber, H., Wächtershäuser, G., Rose, D. & Stetter, K. O. Pyrite formation linked with hydrogen evolution under anaerobic conditions. *Nature* **346**, 742–744 (1990).
33. Wächtershäuser, G. In *Geomicrobiology: Molecular and Environmental Perspective* Ch. Chapter 1, 1–35 (Springer, 2010).
34. Rickard, D. & Luther, G. W. 3rd Chemistry of iron sulfides. *Chem. Rev.* **107**, 514–562 (2007).

35. Hoatson, D. M. et al. Late Archean Lake Harris Komatiite, Central Gawler Craton, South Australia: Geologic setting and geochemistry. *Econ. Geol.* **100**, 349–374 (2005).
36. Teles, G., Chemale, F. & de Oliveira, C. G. Paleoarchean record of the detrital pyrite-bearing, Jacobina Au–U deposits, Bahia, Brazil. *Precambrian Res* **256**, 289–313 (2015).
37. Caban-Acevedo, M. et al. Ionization of high-density deep donor defect states explains the low photovoltage of iron pyrite single crystals. *J. Am. Chem. Soc.* **136**, 17163–17179 (2014).
38. Zebarjad, M., Jamali-Sheini, F. & Yousefi, R. Electrodeposition of nanostructured FeS_2 films: the effect of Sn concentrations on the optoelectronic performance. *Solid State Sci.* **120**, 106722 (2021).
39. Mateo-Marti, E., Galvez-Martinez, S., Gil-Lozano, C. & Zorzano, M.-P. Pyrite-induced Uv-photocatalytic abiotic nitrogen fixation: implications for early atmospheres and life. *Sci. Rep.* **9**, 15311 (2019).
40. Tributsch, H., Fiechter, S., Jokisch, D., Rojas-Chapana, J. & Ellmer, K. Photoelectrochemical power, chemical energy and catalytic activity for organic evolution on natural pyrite interfaces. *Orig. Life Evol. Biosph.* **33**, 129–162 (2003).
41. Cody, G. D. et al. Primordial carbonylated iron-sulfur compounds and the synthesis of pyruvate. *Science* **289**, 1337–1340 (2000).
42. Zhang, X. V. & Martin, S. T. Driving parts of Krebs cycle in reverse through mineral photochemistry. *J. Am. Chem. Soc.* **128**, 16032–16033 (2006).
43. Novikov, Y. & Copley, S. D. Reactivity landscape of pyruvate under simulated hydrothermal vent conditions. *Proc. Natl Acad. Sci. USA.* **110**, 13283–13288 (2013).
44. Wang, W. et al. Photocatalytic reversible amination of α-Keto acids on a ZnS surface: implications for the prebiotic metabolism. *Chem. Commun.* **48**, 2146–2148 (2012).
45. Antonov, V. N., Germash, L. P., Shpak, A. P. & Yaresko, A. N. Electronic structure, optical and X-ray emission spectra in FeS_2. *Phys. Status Solidi B* **246**, 411–416 (2009).
46. Hu, J., Zhang, Y., Law, M. & Wu, R. First-principles studies of the electronic properties of native and substitutional anionic defects in bulk iron pyrite. *Phys. Rev. B* **85**, 085203 (2012).
47. Hulliger, F. & Mooser, E. Semiconductivity in pyrite, marcasite and arsenopyrite phases. *J. Phys. Chem. Solids* **26**, 429–433 (1965).
48. Schena, T., Bihlmayer, G. & Blügel, S. First-principles studies of FeS_2 using many-body perturbation theory in the $\boldsymbol{G_0W_0}$ approximation. *Phys. Rev. B* **88**, 235203 (2013).
49. Choi, S. G. et al. Pseudodielectric function and critical-point energies of iron pyrite. *Phys. Rev. B* **86**, 115207 (2012).
50. Perdew, J. P., Burke, K. & Ernzerhof, M. Generalized gradient approximation made simple. *Phys. Rev. Lett.* **77**, 3865–3868 (1996).
51. Kresse, G. & Joubert, D. From ultrasoft pseudopotentials to the projector augmented-wave method. *Phys. Rev. B* **59**, 1758–1775 (1999).
52. Caldeweyher, E., Mewes, J.-M., Ehlert, S. & Grimme, S. Extension and evaluation of the D4 London-dispersion model for periodic systems. *Phys. Chem. Chem. Phys.* **22**, 8499–8512 (2020).
53. Hjorth Larsen, A. et al. The atomic simulation environment-a python library for working with atoms. *J. Phys.: Condens. Matter* **29**, 273002 (2017).
54. Lavskaya, Y. V. et al. Valence band of the chlorinated Fullerene $C_{60}Cl_{30}$ probed by photoemission and X-ray Emission Spectroscopy. *J. Mol. Struct.* **921**, 264–267 (2009).

Acknowledgements

This work was supported by the National Natural Science Foundation of China (Grant No. 21931008, S. C.), the National Key R&D Program of China (Grant No. 2021YFA1200301, S. C), and the Shanghai Pilot Program for Basic Research-Shanghai Jiao Tong University (21TQ1400219).

Author contributions

Y.F. conceived the idea and led the project. R.L. performed the SEM, XRD, photocatalysis measurements, and HPLC enantiomer measurements. Q.D. and L.H. worked on the structural characterization through HRTEM; T.O., R.L., and Y.F. contributed to the theoretical calculations; R.L., Y.F., and S.C. contributed to the analysis of the mechanism and the preparation of the manuscript.

Competing interests

The authors declare no competing interests.

Additional information

Supplementary information The online version contains supplementary material available at https://doi.org/10.1038/s41467-024-54481-x.

Correspondence and requests for materials should be addressed to Shunai Che or Yuxi Fang.

Peer review information *Nature Communications* thanks the anonymous reviewer(s) for their contribution to the peer review of this work. A peer review file is available.